Journal of
Applied Crystallography
ISSN 0021-8898
Editor: **Gernot Kostorz**

Structure of nanocrystalline $MgFe_2O_4$ from X-ray diffraction, Rietveld and atomic pair distribution function analysis

Milen Gateshki, Valeri Petkov, Swapan K. Pradhan and Tom Vogt

Journal of
Applied
Crystallography
ISSN 0021-8898

Received 23 May 2005
Accepted 29 July 2005

Structure of nanocrystalline $MgFe_2O_4$ from X-ray diffraction, Rietveld and atomic pair distribution function analysis

Milen Gateshki,[a]* Valeri Petkov,[a]* Swapan K. Pradhan[b] and Tom Vogt[c,d]

[a]Department of Physics, Central Michigan University, Mt Pleasant, MI 48859, USA, [b]Department of Physics, The University of Burdwan, Golapbag, Burdwan 713104, India, [c]Department of Physics, Brookhaven National Laboratory, Upton, NY 11973, USA, and [d]Nanocenter and Department of Chemistry and Biochemistry, University of South Carolina, SC 29208, USA. Correspondence e-mail: gates1m@cmich.edu, petkov@phy.cmich.edu

The three-dimensional structure of nanocrystalline magnesium ferrite, $MgFe_2O_4$, prepared by ball milling, has been determined using synchrotron radiation powder diffraction and employing both Rietveld and atomic pair distribution function (PDF) analysis. The nanocrystalline ferrite exhibits a very limited structural coherence length and a high degree of structural disorder. Nevertheless, the nanoferrite possesses a very well defined local atomic ordering that may be described in terms of a spinel-type structure with Mg^{2+} and Fe^{3+} ions almost randomly distributed over its tetrahedral and octahedral sites. The new structural information helps explain the material's unusual magnetic properties.

1. Introduction

In recent years, magnetic nanostructured materials have attracted much attention because of their unique and novel properties and a wide variety of potential applications, such as information storage, color imaging, bioprocessing and magnetic refrigeration (Leslie-Pelecky & Rieke, 1996). Some important examples of magnetic nanomaterials are the nanocrystalline ferrites (Vestal & Zhang, 2004; Liu *et al.*, 2000; Morrison *et al.*, 2004; Pannaparayil *et al.*, 1988; Wang *et al.*, 2004; Chen & Zhang, 1998), in particular $MgFe_2O_4$. Crystalline magnesium ferrite is a soft magnetic material (Willey *et al.*, 1993), which is used in catalysis (Coquay *et al.*, 2002; Astorino *et al.*, 1994), microwave devices (Sugimoto, 1999) and fuel cells (Okawa *et al.*, 2004). In nanocrystalline magnesium ferrite, many of the useful properties of its crystalline counterpart, such as, for example, magnetization, are enhanced. In addition, nanocrystalline magnesium ferrite has been found to exhibit some unusual magnetic properties, such as superparamagnetism and a non-collinear ordering of the magnetic moments of Fe^{3+} ions, known as spin canting (Šepelák *et al.*, 2003, 2002). Owing to its nanocrystalline nature and useful properties, the material shows a good potential for novel applications in humidity and oxygen sensing, photoelectronics and drug delivery (Chen *et al.*, 2000; Konishi *et al.*, 2004; Goldman, 1990). A good understanding of the useful properties of nanocrystalline magnesium ferrite, in particular the magnetic ones, requires detailed knowledge of its three-dimensional structure, including the distribution of the magnetically active iron cations at the atomic scale, the mean-square displacement of the atoms from their average positions and the length of structural coherence. The first of these structural parameters determines the magnetization properties, the second has a direct impact on the sign and magnitude of the exchange interactions between the magnetic moments of Fe^{3+} cations and thus impacts the onset of magnetic ordering, also known as the Néel magnetic ordering temperature, and the third is known to influence the magnetic coherence length known as the magnetic domain size. Such detailed structural information can be obtained only by diffraction techniques, which give a volume-averaged picture of the atomic ordering. In contrast, imaging techniques such as transmission electron microscopy (TEM) or atomic force microscopy (AFM) reveal only structural features projected down one axis or onto a surface.

We report here a structural study of nanocrystalline $MgFe_2O_4$ ferrite prepared by ball milling. We find that its atomic arrangement may be well described in terms of a spinel-type structure, with the distribution of Fe^{3+} and Mg^{2+} cations over its tetrahedral and octahedral sites close to random. The spinel-type arrangement, however, exhibits a considerable local structural disorder and becomes poorly defined at distances longer than 50–60 Å. The new structural information helps explain the material's magnetic properties.

2. Experimental

2.1. Sample preparation

Nanocrystalline $MgFe_2O_4$ was prepared by high-energy ball milling of stoichiometric amounts of MgO and α-Fe_2O_3 using a planetary ball mill with 30 hardened chrome steel balls of 10 mm diameter at a BPMR (ball-to-powder mass ratio) of 40:1. The rotation speed of the disk was 325 r.p.m. and that of

the vial 475 r.p.m. More details on the preparation are given by Pradhan *et al.* (2005). In order to reveal better the steps in the transformation of the two-phase mixture of MgO and α-Fe_2O_3 to a nanocrystalline material, we prepared and studied several samples milled for 1, 3, 5, 9, 11 and 15 h. In addition, some of the sample milled for 9 h was annealed at different temperatures (from 873 to 1473 K) for 5 h until it turned into a crystalline $MgFe_2O_4$ ferrite. The starting mixture of MgO and α-Fe_2O_3, the products of milling for different periods of time and the thermally treated samples were characterized by powder X-ray diffraction.

2.2. Powder X-ray diffraction experiments

Powder X-ray diffraction experiments were carried out on a Philips X'Pert diffractometer using Cu $K\alpha$ radiation. The samples were loaded into the shallow cavity of a glass sample holder and the measurements were carried out in reflection geometry. The diffraction patterns were collected in steps of $2\theta = 0.02^\circ$. The counting time was 15 s per step. Experimental powder X-ray diffraction (XRD) patterns for the starting mixture of MgO and α-Fe_2O_3, and the products resulting from its milling for several time intervals, are shown in Fig. 1. As can be seen in the figure, nanophase $MgFe_2O_4$ spinel forms already at the early stages of the milling process (3–5 h) and the amount increases gradually with milling time. At the same time the Bragg peaks of the starting mixture disappear as a result of its transformation into a single-phase nanomaterial. Traces of α-Fe_2O_3 are, however, seen even in the diffraction pattern for the sample milled for 11 h, showing that the degree of transformation is very close to but not exactly 100%. After 15 h of ball milling the relative abundance of α-Fe_2O_3 is seen to increase slightly, most probably as a result of decomposition of the already formed nanophase. Therefore, our further studies on nanocrystalline $MgFe_2O_4$ were carried out on the sample obtained by ball milling for 11 h, showing an almost negligible amount of the precursor material. No traces of metal Fe particles are observed in any of the diffraction patterns presented in Fig. 1. Such particles are sometimes found in materials prepared by ball milling employing steel vials and balls (Šepelák *et al.*, 2002) but the preparation route we followed prevented their appearance in our samples.

Experimental X-ray diffraction patterns for the 9 h ball-milled material and the products of its annealing at several temperatures are shown in Fig. 2. The peaks in the diffraction patterns of the thermally treated samples become sharper with annealing temperature as a result of the gradually improving crystallinity. The traces of α-Fe_2O_3 become less visible with annealing and completely disappear with the sample treated at 1473 K. This sample is stoichiometric $MgFe_2O_4$, as shown by our diffraction and chemical analyses. It is also almost perfectly crystalline, since the Bragg peaks in its diffraction pattern appear almost as sharp as those in the diffraction pattern of an Si standard reference material (NIST 640c). To obtain data with quality more suitable for structure studies we subjected the sample milled for 11 h, hereafter referred to as nanocrystalline $MgFe_2O_4$, to synchrotron radiation scattering experiments. Crystalline $MgFe_2O_4$, obtained as described above, was also measured and used as a reference sample.

2.3. Synchrotron radiation scattering experiments

Synchrotron radiation scattering experiments were carried out at beamline X7A at the National Synchrotron Light Source, Brookhaven National Laboratory, using X-rays of energy 30.9883 keV ($\lambda = 0.4001$ Å) at room temperature. The higher-energy X-rays were used to extend the region of reciprocal space covered, which is important for the success of the atomic pair distribution function (PDF) technique introduced

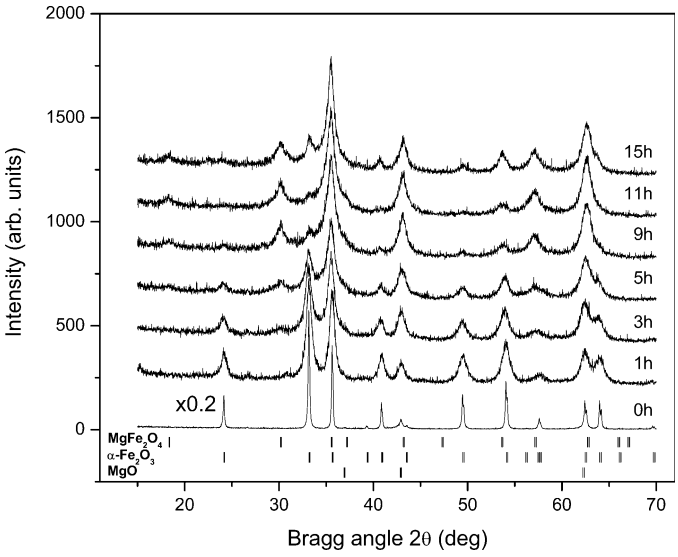

Figure 1
Experimental X-ray powder diffraction patterns for a mixture of MgO and α-Fe_2O_3 (0 h) and the products of its milling carried out for different time intervals. The positions of the Bragg peaks of MgO, α-Fe_2O_3 and the emerging nanocrystalline $MgFe_2O_4$ are given as bars in the lower part of the plot.

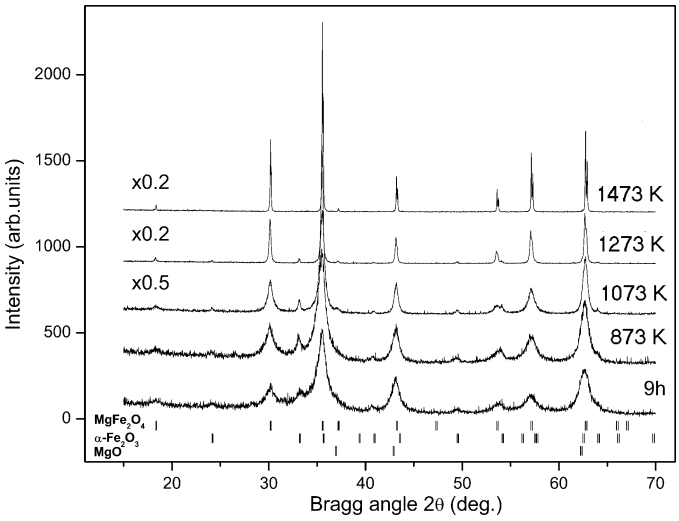

Figure 2
Experimental X-ray powder diffraction patterns for the 9 h milled sample and the products of its annealing at temperatures ranging from 873 to 1473 K. The positions of the Bragg peaks of MgO, α-Fe_2O_3 and $MgFe_2O_4$ are given as bars in the lower part of the plot.

later on. This setup, coupled with the good reciprocal-space resolution and high flux at X7A, also allowed the collection of data of a quality suitable for Rietveld analysis. The samples were loaded into thin aluminium frames and sealed with Kapton foils. The experiments were carried out in symmetric transmission geometry. Scattered radiation was collected with an intrinsic germanium detector connected to a multi-channel analyzer. Several diffraction runs were conducted with each of the samples measured and the collected diffraction patterns were averaged out to improve the statistical accuracy of the diffraction data. The resulting synchrotron radiation diffraction patterns for crystalline and nanocrystalline $MgFe_2O_4$ are shown in Fig. 3.

2.4. DSC characterization of the magnetic state of nanocrystalline and crystalline $MgFe_2O_4$

The magnetic state of crystalline and nanocrystalline $MgFe_2O_4$ samples was assessed by measuring the temperature at which they order magnetically. The onset of magnetic ordering in ferrites is usually a second-order phase transition. The corresponding, so-called Néel, transition temperature can be accurately detected by differential scanning calorimetry (DSC) experiments because of the increase of the magnetic component of the specific heat in the vicinity of the phase transition (O'Neill *et al.*, 1992; Stanley, 1971). The DSC measurements were carried out on a Perkin–Elmer DSC-7 instrument. The results are shown in Fig. 4. The DSC data for crystalline $MgFe_2O_4$ show a well expressed thermal anomaly around 673 K. As previous studies on crystalline magnesium ferrite have shown (O'Neill *et al.*, 1992; Antao *et al.*, 2005), the anomaly is due to a disorder–order (paramagnetic at higher temperature to antiferromagnetic at lower temperature) magnetic phase transition. The observed Néel temperature of ~673 K is typical for crystalline magnesium ferrites with a very high degree of inversion (O'Neill *et al.*, 1992), *i.e.* having an almost equal number of Fe^{3+} ions occupying the octahedral and tetrahedral sites in the spinel lattice shown in Fig. 5. The result suggests that our crystalline $MgFe_2O_4$ sample is also likely to exhibit a high degree of inversion.

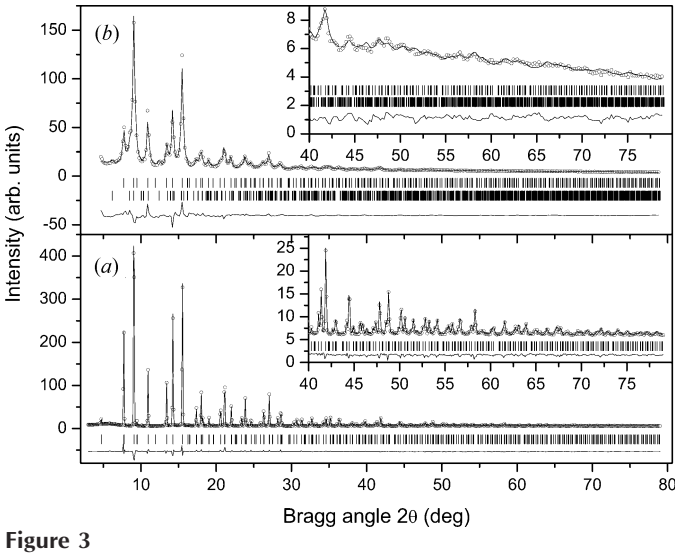

Figure 3
Experimental (symbols) and calculated (solid line) synchrotron radiation diffraction patterns for (*a*) crystalline and (*b*) nanocrystalline $MgFe_2O_4$. The calculated patterns are obtained through Rietveld refinement. The reliability factors achieved are $R_{wp} = 9.5$ and 13.1% for the crystalline and nanocrystalline ferrite, respectively. The positions of the Bragg peaks of the spinel structure are given in the lower part in (*a*) and (*b*) as bars. In addition, the positions of the Bragg peaks of a minor second phase, α-Fe_2O_3, seen in the diffraction pattern of nanocrystalline $MgFe_2O_4$, are given as bars in (*b*).

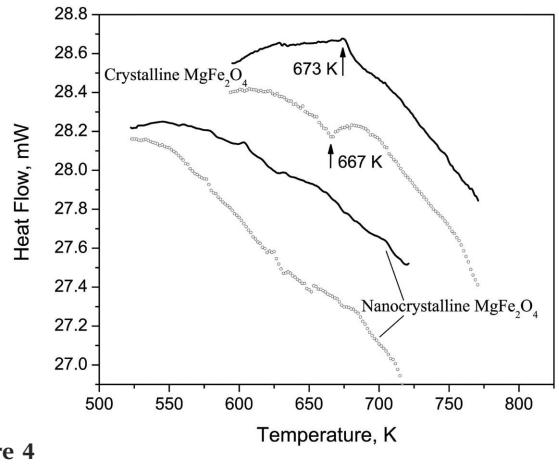

Figure 4
DSC scans for crystalline and nanocrystalline $MgFe_2O_4$. Arrows point to the observed thermal anomalies due to the antiferromagnetic (low *T*) to paramagnetic (high *T*) phase transition in the crystalline sample. Scans taken while heating the samples are presented as solid lines and those while cooling as symbols.

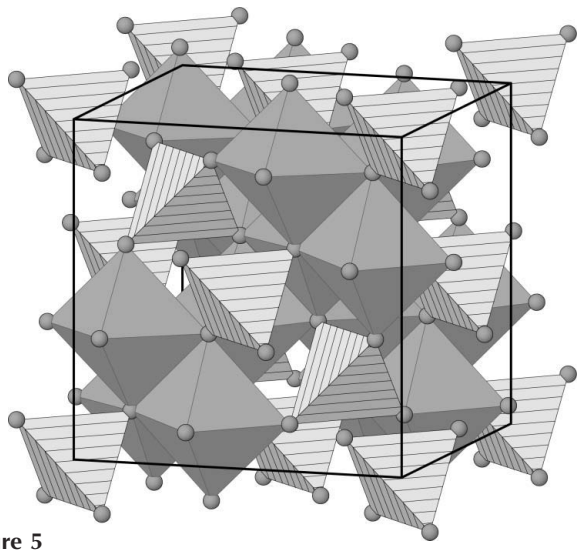

Figure 5
Fragment of the spinel-type structure occurring with iron magnesium ferrite. The cubic unit cell is outlined with thick solid lines. Cations such as Mg^{2+} and Fe^{3+} are known to occupy the centers of tetrahedra (hatched), known as (*A*) sites, and octahedra, known as [*B*] sites. O atoms (small circles) are located on the vertices of both polyhedral units. The general chemical formula of magnesium ferrite is usually given as $(Mg_{1-x}Fe_x)[Mg_xFe_{2-x}]O_4$, where $(Mg_{1-x}Fe_x)$ and $[Mg_xFe_{2-x}]$ represent the tetrahedral (*A*) and octahedral [*B*] sites of the spinel-type structure, respectively. The parameter *x* is the so-called degree of inversion, defined as the fraction of tetrahedral sites occupied by Fe^{3+} cations (O'Neill *et al.*, 1992). A 'normal'-type spinel corresponds to $x = 0$, an 'inverse'-type to $x = 1$ and a 'random'-type to $x = 2/3$.

As can also be seen in Fig. 4, the DSC data for the nanocrystalline ferrite do not show any anomaly that could suggest the onset of magnetic ordering. As previous studies have shown, the presence of a high degree of structural disorder usually reduces the strength of the magnetic interactions and the onset of magnetic ordering is shifted to very low temperatures, if such an onset takes place at all (Ahn *et al.*, 2003). The fact that nanocrystalline magnesium ferrite shows no apparent magnetic ordering from room temperature up to 723 K suggests that the material is likely to exhibit a considerable structural disorder. It is worth noting that other studies have also reported the lack of spontaneous magnetic ordering in nanocrystalline $MgFe_2O_4$ obtained by ball milling (Šepelák *et al.*, 2003).

3. Results

As can be seen in Fig. 3, the synchrotron radiation pattern for crystalline $MgFe_2O_4$ exhibits very sharp Bragg peaks up to very high diffraction angles, reflecting the material's good crystallinity. The peaks could be easily indexed in a cubic unit cell and explained in terms of a spinel-type structure, as our subsequent analyses show. The Bragg peaks in the XRD patterns for nanocrystalline $MgFe_2O_4$ are rather broad and merge into a slowly oscillating diffuse component at diffraction angles as low as 40°. Such diffraction patterns are typical for materials with considerable local structural disorder and are difficult to tackle by traditional techniques for structure determination from powder data. For this reason, we also considered the experimental powder diffraction data in terms of the corresponding atomic PDFs. As the pioneering study of Toby & Egami (1992) and several subsequent studies (Egami & Billinge, 2003; Billinge & Kanatzidis, 2004) have shown, the atomic PDF is a useful technique for studying the atomic arrangement in crystalline as well as substantially disordered materials.

In our study we employed the widely used reduced PDF, $G(r)$, defined as

$$G(r) = 4\pi r\big[\rho(r) - \rho_0\big], \tag{1}$$

where $\rho(r)$ and ρ_0 are the local and average atomic number densities, respectively, and r is the radial distance. The PDF $G(r)$ is the Fourier transform of the experimentally observable total structure function, $S(Q)$, *i.e.*

$$G(r) = \frac{2}{\pi}\int_{Q=o}^{Q_{\max}} Q[S(Q) - 1]\sin(Qr)\,\mathrm{d}Q, \tag{2}$$

where Q is the magnitude of the wavevector [$Q = 4\pi(\sin\theta)/\lambda$], 2θ is the angle between the incoming and outgoing radiation beams, and λ is the wavelength of the radiation used. The structure function is related to the coherent part of the powder diffraction data as follows:

$$S(Q) = 1 + \Big[I^{\mathrm{coh}}(Q) - \textstyle\sum c_i\big|f_i(Q)\big|^2\Big]\Big/\big|\textstyle\sum c_i f_i(Q)\big|^2, \tag{3}$$

where $I^{\mathrm{coh}}(Q)$ is the coherent scattering intensity per atom in electron units and c_i and f_i are the atomic concentration and X-ray scattering factor, respectively, for the atomic species of type i (Klug & Alexander, 1974; Egami & Billinge, 2003; Keen, 2001). The great advantage of the atomic PDF technique is that it takes into account all components of the experimental diffraction data, including Bragg peaks and diffuse scattering. In this way, the PDF reflects both the longer-range atomic structure, manifested in the Bragg peaks, and the local structural imperfections, manifested in the diffuse component of the diffraction pattern (Egami & Billinge, 2003). Note that the traditional techniques for structure determination from powder diffraction data, such as Rietveld analysis, rely on the Bragg peaks in the diffraction data alone. Furthermore, by accessing higher values of Q, experimental $G(r)$ functions with improved real-space resolution can be obtained and hence quite fine structural features can be revealed (Petkov *et al.*, 1999). In fact, data at high Q values ($Q > 10$ Å^{-1}) are critical to the success of PDF analysis (Toby & Egami, 1992). For this reason, our synchrotron radiation diffraction patterns were collected to Q values as high as 20 Å^{-1}, which is close to the limit of Q values that can be reached at beamline X7A. The experimental PDFs for crystalline and nanocrystalline $MgFe_2O_4$ are shown in Fig. 6. They were obtained from the synchrotron radiation diffraction patterns presented in Fig. 3 with the help of the program *RAD* (Petkov, 1989), applying all necessary corrections for flux, absorption, background and Compton scattering. As can be seen in the figure, the experimental PDF for crystalline $MgFe_2O_4$ is rich in well defined structural features, extending to very high real-space distances, as it should be with a perfectly ordered and three-dimensional periodic material. The PDF for the nanocrystalline ferrite is also rich in well defined features, but they are broader than those in the PDF for the crystalline ferrite and

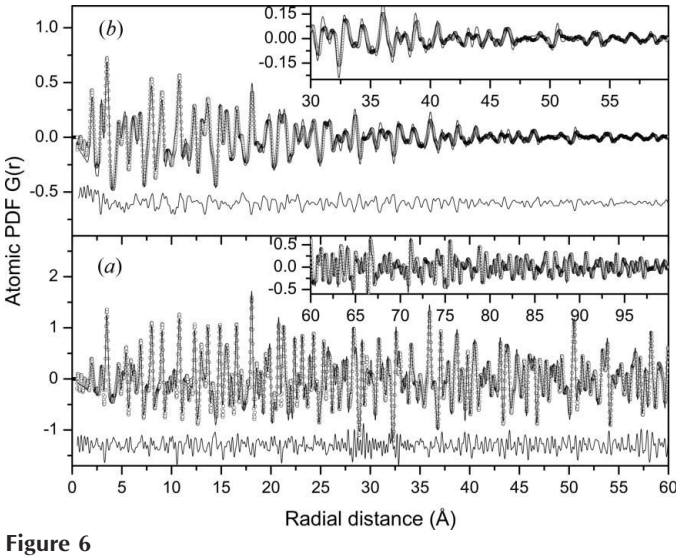

Figure 6
Experimental (symbols) and model (lines) atomic PDFs $G(r)$ for (*a*) crystalline and (*b*) nanocrystalline $MgFe_2O_4$. The model PDFs are calculated through a least-squares fitting procedure as explained in the text. The structural parameters corresponding to the best fit achieved are listed in Table 1. The residual difference between the experimental and model data is given in the lower part of the plots. The corresponding reliability (goodness-of-fit) parameters are R_w = 16.7 and 20.2% for the crystalline and nanocrystalline ferrite, respectively.

vanish at ~60 Å. Obviously, the nanostructured ferrite has an atomic arrangement well defined at nanoscale distances but lacks the extended and perfect order of conventional bulk crystals. This observation, and the findings of similar independent studies (Šepelák *et al.*, 2003), suggest that imperfect atomic ordering may be the reason for the lack of magnetic ordering in nanocrystalline $MgFe_2O_4$. Our subsequent Rietveld and PDF analyses explore this suggestion and reveal the structure–property relationship in nanocrystalline $MgFe_2O_4$ in more detail.

4. Discussion

To determine the essential structural features of nanocrystalline $MgFe_2O_4$, we analyzed its synchrotron radiation diffraction pattern employing Rietveld analysis first. The Rietveld (1969) analysis is a well established technique for crystal structure determination and refinement from powder diffraction data. The method employs a least-squares procedure to compare Bragg intensities and those calculated from a plausible structural model. The structural parameters of the model are then adjusted until the best fit to the experimental diffraction data is achieved. The progress of the fit is assessed by computing various agreement factors, the most frequently used being (Young, 1996)

$$R_{\rm wp} = \left[\frac{\sum w_i (y_i^{\rm obs} - y_i^{\rm calc})^2}{\sum w_i (y_i^{\rm obs})^2}\right]^{1/2} \qquad (4)$$

where $y_i^{\rm obs}$ and $y_i^{\rm calc}$ are the observed and calculated data points, and w_i are weighting factors taking into account the statistical accuracy of the diffraction experiment. The Rietveld analysis of the diffraction pattern of nanocrystalline $MgFe_2O_4$ was carried out with the help of the program *FullProf* (Rodríguez-Carvajal, 1993). Crystalline $MgFe_2O_4$ was used as a reference sample and its synchrotron radiation diffraction pattern was also subjected to Rietveld analysis. In the course of the analysis, the two types of cations (Mg^{2+} and Fe^{3+}) were allowed to occupy either of the two distinct crystallographic positions (A) and [B] in the spinel lattice (see Fig. 5). The occupancy factors of the cation positions were constrained so as to preserve the stoichiometric composition of the material, $MgFe_2O_4$. The results of the Rietveld analyses are presented in Fig. 3. As can be seen in the figure, a single-phase model based on the spinel-type structure reproduces the experimental data for the crystalline ferrite very well. The diffraction pattern of nanocrystalline $MgFe_2O_4$ is reproduced adequately by a two-phase model based on a mixture of a majority ferrite phase, $MgFe_2O_4$, and a minority (8 wt%) α-Fe_2O_3 phase. The refined structural parameters for the two studied materials are listed in Table 1. The data reveal that both crystalline and nanocrystalline $MgFe_2O_4$ ferrites posses a spinel-type structure with the cubic lattice shown in Fig. 5. Crystalline $MgFe_2O_4$ is almost an inverse spinel ($x \simeq 0.93$), while nanocrystalline $MgFe_2O_4$ is close to random ($x \simeq 0.64$). A closer examination of the table, however, shows that the Rietveld analysis yielded negative mean-square (m.s.) atomic displacements ('thermal factors') for the O atoms. Such unphysical displacement parameters are known to result from Rietveld analyses of powder diffraction patterns of materials with considerable intrinsic disorder. The problem stems from the inability of the technique to handle properly diffraction patterns showing both broad Bragg peaks and pronounced diffuse scattering. To overcome the problem, we attempted the same structural models, but this time employing the experimental PDFs as quantities guiding the refinement process. Our reasoning was based on the work of Jeong *et al.* (1999), pointing out the advantages of using atomic PDFs for the assessment of m.s. atomic displacements in materials with considerable local structural disorder. Similarly to Rietveld analysis, the PDF technique employs a least-squares procedure to compare experimental and model data (PDF) calculated from a plausible structural model. The structural parameters of the model (unit cell constants, atomic coordinates and thermal factors) are adjusted until the best possible fit to the experimental data is achieved. The progress of the refinement is assessed by computing an agreement factor, $R_{\rm w}$;

$$R_{\rm w} = \left[\frac{\sum w_i (G_i^{\rm exp} - G_i^{\rm calc})^2}{\sum w_i (G_i^{\rm exp})^2}\right]^{1/2}, \qquad (5)$$

where $G^{\rm exp}$ and $G^{\rm calc}$ are the experimental and calculated PDFs, respectively, and w_i are weighting factors reflecting the statistical quality of the individual data points. When comparing with the experiment, the model PDFs are convoluted with a *Sinc* function (Billinge, 1998) of the type

$$P(r) = \sin(Q_{\rm max} r)/r \qquad (6)$$

to take into account the finite $Q_{\rm max}$ of the diffraction data (in our case $Q_{\rm max} = 20$ Å^{-1}).

The results of the PDF analyses are depicted in Fig. 6. They were carried out with the help of the program *PDFFIT* (Proffen & Billinge, 1999) and for both materials were based on a single-phase model featuring a spinel-type structure. The inclusion of a minor second phase (α-Fe_2O_3) neither improved nor deteriorated the PDF analysis of the nanocrystalline

Table 1
Structural parameters for crystalline and nanocrystalline $MgFe_2O_4$ obtained through Rietveld and PDF analyses.

The structure model is cubic ($Fd\bar{3}m$ space group), and Mg^{2+} and Fe^{3+} cations occupy Wyckoff positions 8*a* [tetrahedral sites (A)] and 16*d* (octahedral sites [B]). The fractional coordinates of (A) and [B] positions are ($\frac{1}{8}, \frac{1}{8}, \frac{1}{8}$) and ($\frac{1}{2}, \frac{1}{2}, \frac{1}{2}$), respectively. O atoms occupy Wyckoff position 32*e* with fractional coordinates (x, x, x). The degree of inversion, x, is defined as the percentage of Fe^{3+} cations occupying the tetrahedral (A) positions in the cubic lattice.

	Crystalline		Nanocrystalline	
	Rietveld	PDF	Rietveld	PDF
a (Å)	8.374 (1)	8.373 (1)	8.393 (1)	8.390 (1)
x	0.256 (1)	0.256 (1)	0.254 (1)	0.254 (1)
$B_{(A)}$ (Å^2)	0.2 (1)	0.3 (1)	0.6 (1)	1.0 (1)
$B_{[B]}$ (Å^2)	0.2 (1)	0.4 (1)	1.2 (2)	1.3 (1)
$B_{\rm O}$ (Å^2)	0.5 (1)	0.8 (1)	−0.3 (1)	1.4 (1)
Inversion (%)	93 (1)	94 (1)	64 (1)	70 (1)
$R_{\rm wp}$ (%)	9.5	16.7	13.0	20.2

ferrite and therefore such a second phase was not considered. The structural parameters of crystalline and nanocrystalline $MgFe_2O_4$ resulting from the PDF analyses are listed in Table 1. In the case of crystalline $MgFe_2O_4$ the Rietveld and PDF-based analyses yielded very similar results for the lattice constants, the atomic coordinates and the degree of inversion. The agreement well documents the fact that the atomic PDF provides a reliable quantitative basis for structure determination. The m.s. atomic displacements yielded by the PDF analysis, however, appear somewhat larger than the Rietveld results. This difference may be due to the presence of some residual local disorder in our crystalline sample as a result of insufficient annealing. In the case of nanocrystalline $MgFe_2O_4$, the Rietveld and PDF-based analyses also yielded very similar results for the lattice constants, the atomic coordinates and the degree of inversion. The m.s. atomic displacements resulting from the PDF analysis are, in contrast to the Rietveld results, positive and thus more realistic. They are two to three times as large as those in the $MgFe_2O_4$ crystal (for the sake of consistency the comparison is made on the basis of the PDF results), indicating the presence of a very substantial local structural disorder in the nanostructured material. As we show later, this substantial local structural disorder can explain well many of the unusual magnetic properties of nanocrystalline $MgFe_2O_4$. Here it may be noted that the agreement factors achieved with the PDF refinements appear somewhat higher than those resulting from the Rietveld refinement of diffraction data in reciprocal space (see Table 1). This difference reflects the fact that an atomic PDF differs from the corresponding XRD pattern and is a quantity that is much more sensitive to the local atomic ordering in materials. As a result, R_w values greater than 20% are common for PDF refinements, even for well crystallized materials (Gateshki *et al.*, 2004; Petkov *et al.*, 2000, 2002). The inherently higher absolute values of the goodness-of-fit factors resulting from PDF-based refinements do not affect their functional purpose as a residual quantity that must be minimized to find the best fit and as a quantity allowing differentiation between competing structural models. It may also be noted that when the atomic pair correlation function, $g(r)$, defined as $g(r) = \rho(r)/\rho_0$, is used to guide a refinement of a structural model, the resulting agreement factors R_w are significantly lower than those reported from a refinement based on the corresponding PDF $G(r)$ and very close to the values of the agreement factors reported from Rietveld analyses. However, we prefer to work with the PDF $G(r)$ and not $g(r)$, since the former scales with the radial distance r [see the multiplicative factor in the definition of $G(r)$, equation (1)] and is thus more sensitive to the longer-range atomic correlations.

To determine the structural coherence length (sometimes also referred to as the average size of coherently scattering domains) in the nanocrystalline ferrite we proceeded as follows. First, we determined the FWHM (full width at half-maximum) of the Bragg peaks located between 7.5 and 11.5° (2θ) in the diffraction patterns for the crystalline and nanocrystalline material. The values we obtained were 0.16 and 0.40°, respectively. The sample-related contribution to the FWHM was estimated on the basis the formula (Azároff & Buerger, 1958)

$$B_{\rm sample} = (B^2_{\rm meas} - B^2_{\rm inst})^{1/2}, \tag{7}$$

where $B_{\rm meas}$ is the FWHM of the peaks in the diffraction pattern of the nanocrystalline ferrite and $B_{\rm inst}$ is the FWHM of those in the diffraction pattern of the crystalline ferrite used here as a reference sample. The average size of the coherently scattering domains, L, was estimated using the Scherrer equation (Azároff & Buerger, 1958):

$$B_{\rm sample} = K\lambda/L\cos\theta, \tag{8}$$

where $K = 0.93$ and λ is the wavelength of the radiation used. This approach yielded an L value of the order of 60 Å. We then estimated the same quantity on the basis of the experimental PDF data. A visual inspection of the data in Fig. 6(*b*) clearly shows that the peaks in the data, each corresponding to a particular atomic pair/coordination sphere, decay almost to zero at approximately 60 Å.[1] Clearly, at distances shorter than 60 Å, the atomic arrangement is well defined, while at distances longer than 60 Å, it is not so well defined. Hence, the real-space distance of 60 Å is a good measure of the length of structural coherence in nanocrystalline $MgFe_2O_4$. As an independent check of the above estimates, we applied the theory developed by Ergun & Schehl (Ergun, 1970; Ergun & Schehl, 1973), who suggested that the presence of local structural disorder causes an exponential decay in the PDF data of the type

$$f(r) = \exp(-\alpha r), \tag{9}$$

where $2/\alpha$ is the average length of structural coherence. Using the crystalline ferrite as a reference for an almost disorder-free material and treating the corresponding PDFs in the way outlined by Qiu *et al.* (2004), we obtained α of the order of 0.04 Å^{-1}. This value of α yielded a structural coherence length of the order of 50 Å. The good agreement between the outcomes of the three independent approaches gives us the confidence to state that the length of structural coherence in nanocrystalline $MgFe_2O_4$ is limited to only ~50–60 Å.

In summary, the results of our structural studies show that both crystalline and nanocrystalline $MgFe_2O_4$ possess a spinel-type structure. The crystalline ferrite has a very high degree of inversion ($x \simeq 0.93$–0.94), as both the Rietveld and PDF analyses reveal. The cation distribution in the spinel structure of the nanocrystalline ferrite is close to random ($x \simeq 0.64$–0.70; see Table 1). Obviously the distribution of cations in ferrites engineered at nanoscales could be different from that in their bulk crystalline counterparts. Furthermore, as our annealing studies showed, that distribution could be tuned up by a

[1] As pointed out by Toby & Egami (1992), some experimental artifacts, such as the finite $Q_{\rm max}$ of the diffraction data and/or the limited resolution in reciprocal space, may considerably smooth out the experimental PDF data at longer real-space distances. Such artifacts are not likely to be responsible for the fast decay exhibited by the experimental PDF data for the nanocrystalline ferrite since, if they were of any importance in our experiment, they would have caused a similar fast decay in the PDF for crystalline $MgFe_2O_4$, which was obtained on the same instrument and under the same experimental conditions. This is clearly not the case, as the data in Fig. 6(*a*) show.

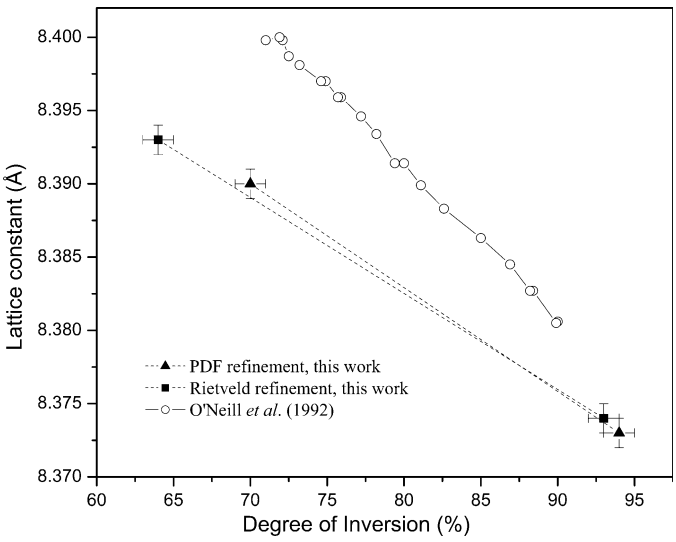

Figure 7
Lattice constants for $MgFe_2O_4$ ferrites as a function of the degree of inversion.

subsequent annealing of the nanocrystalline material. The lattice constants of the two ferrites are slightly different from each other, reflecting the different cationic distributions in the two materials. The values fall within the range of lattice constants reported for other ferrites of similar chemical composition and cationic distribution (see Fig. 7). The good agreement between our results and previous results is further evidence for the reliability of our studies. The most substantial difference between crystalline and nanocrystalline $MgFe_2O_4$ is that, while the former is almost perfectly ordered over very long interatomic distances, the latter possesses an atomic arrangement that is well defined over 50–60 Å only (compare the two sets of PDF data shown in Fig. 6). The much shorter length of structural coherence in the nanostructured ferrite is a result of the presence of a substantial local structural disorder smearing the distinct coordination sequence in the spinel-type lattice at distances longer than 60 Å.

This new structural information helps explain several unusual magnetic properties of the nanocrystalline magnesium ferrite, such as the enhanced magnetization, lack of spontaneous magnetic ordering above room temperature, superparamagnetism and non-collinear ordering of the magnetic moments of Fe ions, as follows. In the spinel-type structure exhibited by magnesium ferrites, Fe^{3+} cations can occupy both the tetrahedral and the octahedral sites shown in Fig. 5. When this occurs, the magnetic moments of Fe^{3+} ions occupying the two different lattice sites point in opposite directions, *i.e.* they are antiparallel to each other as a result of the antiferromagnetic character of their interaction. This exchange interaction is indeed indirect and mediated by the O atoms forming the tetrahedral and octahedral coordination polyhedra of Fe^{3+} ions (Šepelák *et al.*, 2002, 2003; Harrison & Putnis, 1999). In the almost fully inversed crystalline magnesium ferrite studied by us ($x \simeq 0.93$), Mg and Fe ions are distributed over the tetrahedral, (A), and octahedral, $[B]$, sites as follows: $(Mg_{0.07}Fe_{0.93})[Mg_{0.93}Fe_{1.07}]O_4$ (here we follow the notation introduced in Fig. 5). Since Mg ions carry no magnetic moment, the net magnetic moment, μ, in crystalline magnesium ferrite (per formula unit) is entirely due to the uncompensated magnetic moments of the iron ions sitting in the two different lattice sites and interacting in an antiferromagnetic manner, *i.e.* $\mu = 1.07\mu(\mathrm{Fe}) - 0.93\mu(\mathrm{Fe}) = 0.17\mu(\mathrm{Fe})$, where μ(Fe) is the magnetic moment of Fe^{3+} ions. The close to random distribution of cations ($x \simeq 0.64-0.7$) in the nanocrystalline ferrite (see Table 1) results in a net magnetic moment $\mu \simeq 0.6\mu(\mathrm{Fe})$, which well explains the increased magnetization exhibited by this nanostructured material.

To explain the influence of the structural disorder on the magnetic properties of materials the following model Hamiltonian has been considered (Harris *et al.*, 1973; Mukamel & Grinstein, 1982):

$$\mathcal{H} = -\sum (J + \Delta J_{ij}) M_i M_j - D \sum (n_i M_i)^2 - H \sum M_i, \quad (10)$$

where J is the average exchange interaction between nearest magnetic ions (indirect and antiferromagnetic in our case), ΔJ_{ij} represents the exchange-interaction fluctuations due to the structural disorder, D is the strength of the random local magnetocrystalline anisotropy, n_i is the unit vector fixing the random local axis of easy magnetization, and M_i and H are the magnetic moment of the magnetic ion of type i [$i = 1$; $M_1 = \mu(\mathrm{Fe})$ in our case] and the applied field, respectively. According to this model Hamiltonian, the onset of magnetic ordering is highly dependent on the magnitude of the exchange-interaction fluctuations. The higher the magnitude of ΔJ_{ij}, the narrower the temperature region of magnetic ordering. This simple theoretical prediction well accounts for the observed lack of magnetic ordering in nanocrystalline magnesium ferrite at temperatures above room temperature. The strong m.s. displacements of the Fe^{3+} ions (almost three times larger than those in the crystalline ferrite; see Table 1) and the substantial distortions of the oxygen polyhedra (the m.s. displacements of O atoms in the nanoferrite are at least twice those of O atoms in the crystal) are very likely to cause substantial fluctuations in the indirect exchange interactions that can lead to a frustration of the magnetic order to such an extent that it does not emerge spontaneously, as our DSC data and other independent studies (Šepelák *et al.*, 2003) show. Furthermore, the substantial distortions in the tetrahedral and octahedral oxygen environment of Fe ions in the nanocrystalline ferrite are very likely to introduce a strong local magnetocrystalline anisotropy (the second term in the Hamiltonian above) and, hence, make the non-collinear arrangement of the magnetic moments of Fe^{3+} atoms (spin canting) more favorable than the collinear one, as observed experimentally (Šepelák *et al.*, 2002, 2003). Other studies have also associated the spin canting in nanophase ferrites with their inherently disordered structure (Morales *et al.*, 1997).

Finally, the rather small size of coherent structural domains (∼50–60 Å) will definitely impede the formation of extended domains of ordered magnetic moments in $MgFe_2O_4$ nanoferrite. When the magnetic domains are so small, the thermal

energy is sufficient to change the direction of their net magnetic moment in a random manner and the material is a superparamagnet. The fact that superparamagnetism has been observed with nanocrystalline $MgFe_2O_4$ (Šepelák *et al.*, 2002, 2003) then may not come as a big surprise given the rather short range of structural coherence (∼50–60 Å) in the material.

5. Conclusions

The careful analysis of synchrotron radiation diffraction patterns using a conventional Rietveld and a total scattering approach, such as the atomic PDF technique, can provide detailed structural information about nanocrystalline materials. Nanocrystalline magnesium ferrite obtained by ball milling is found to possess a spinel-type structure that may be described in terms of a repetitive cubic unit cell over distances as long as 60 Å. The distribution of the cations over the tetrahedral and octahedral sites in the spinel lattice is close to random ($x \simeq \frac{2}{3}$) and can be changed into an inverse distribution ($x \simeq 1$) by annealing at higher temperatures. The nanocrystalline material does not order magnetically as its crystalline counterpart does and, as other studies have shown, exhibits spin canting and superparamagnetic behavior. Our studies link this behavior to the presence of a substantial local structural disorder manifested by the rather large m.s. displacements of the atoms in the spinel lattice. The latter structural information is best assessed by the PDF approach. This is another demonstration of the great potential of total scattering methods when studying materials with considerable intrinsic disorder and short coherence lengths.

Thanks are due to Y. Lee from BNL for help with the synchrotron radiation experiments and to T. Spassov from Sofia University for assistance with the DSC measurements. The work was supported by the NSF through grant DMR 0304391(NIRT). Beamline X7a at the NSLS is supported by the US Department of Energy through DE-AC02-98-CH0886.

References

Ahn, Y., Choi, E. J. & Kim, E. H. (2003). *Rev. Adv. Mater. Sci.* **5**, 477–480.
Antao, S. M., Hassan, I. & Parize, J. B. (2005). *Am. Mineral.* **90**, 219–228.
Astorino, E., Busca, G., Ramis, G. & Willey, R. J. (1994). *Catal. Lett.* **23**, 353–360.
Azároff, L. V. & Buerger, M. J. (1958). *The Powder Method in X-ray Crystallography*, p. 254. New York: McGraw-Hill.
Billinge, S. J. L. (1998). *Local Structure from Diffraction*, p. 137. New York: Plenum Press.
Billinge, S. J. L. & Kanatzidis, M. G. (2004). *Chem. Commun.* **7**, 749–760.
Chen, N. S., Yang, X. J., Liu, E. S. & Huang, J. L. (2000). *Sens. Actuators B*, **66**, 178–180.
Chen, Q. & Zhang, Z. J. (1998). *Appl. Phys. Lett.* **73**, 3156–3158.
Coquay, P., Peigney, A., De Grave, E., Vandenberghe, R. E. & Laurent, C. (2002). *J. Phys. Chem. B*, **106**, 13199–13210.
Egami, T. & Billinge, S. J. L. (2003). *Underneath the Bragg Peaks: Structural Analysis of Complex Materials*, p. 138. Oxford: Pergamon Press.
Ergun, S. (1970). *Phys. Rev. B*, **1**, 3371–3380.
Ergun, S. & Schehl, R. R. (1973). *Carbon*, **11**, 127–138.
Gateshki, M., Hwang, S.-J., Park, D. H., Ren, Y. & Petkov, V. (2004). *J. Phys. Chem. B*, **108**, 14956–14963.
Goldman, A. (1990). *Modern Ferrite Technology*. New York: Van Nostrand-Reinhold.
Harris, R., Plischke, M. & Zuckermann, M. J. (1973). *Phys. Rev. Lett.* **31**, 160–162.
Harrison, R. J. & Putnis, A. (1999). *Phys. Chem. Minerals*, **26**, 322–332.
Jeong, I.-K., Proffen, T., Mohiuddin-Jacobs, F. & Billinge, S. J. L. (1999). *J. Phys. Chem. A*, **103**, 921–924.
Keen, D. A. (2001). *J. Appl. Cryst.* **34**, 172–177.
Klug, H. P. & Alexander, L. E. (1974). *X-ray Diffraction Procedures for Polycrystalline Materials*, p. 797. New York: Wiley.
Konishi, K., Maehara, T., Kamimori, T., Aono, H., Naohara, T., Kikkawa, H., Watanabe, Y. & Kawachi, K. (2004). *J. Magn. Magn. Mater.* **272–276**, 2428–2429.
Leslie-Pelecky, D. L. & Rieke, R. D. (1996). *Chem. Mater.* **8**, 1770–1783.
Liu, C., Rondinone, A. J. & Zhang, Z. J. (2000). *Pure Appl. Chem.* **72**, 37–45.
Morales, M. P., Serna, C. J., Bodker, F. & Morup, S. (1997). *J. Phys. Condens. Matter*, **9**, 5461–5467.
Morrison, S. A., Cahill, C. L., Carpenter, E. E., Calvin, S., Swaminathan, R., McHenry, M. E. & Harris, V. G. (2004). *J. Appl. Phys.* **95**, 6392–6395.
Mukamel, D. & Grinstein, G. (1982). *Phys. Rev. B*, **25**, 381–388.
Okawa, H., Lee, J. H., Hotta, T., Ohara, S., Takahashi, S., Shibahashi, T. & Yamamasu, Y. (2004). *J. Power Sources*, **131**, 251–255.
O'Neill, H. St C., Annersten, H. & Virgo, D. (1992). *Am. Mineral.* **77**, 725–740.
Pannaparayil, T., Marande, R., Komarneni, S. & Sankar, S. G. (1988). *J. Appl. Phys.* **64**, 5641–5643.
Petkov, V. (1989). *J. Appl. Cryst.* **22**, 387–389.
Petkov, V., Billinge, S. J. L., Heizing, J. & Kanatzidis, M. G. (2000). *J. Am. Chem. Soc.* **122**, 11571–11576.
Petkov, V., Jeong, I.-K., Chung, J. S., Thorpe, M. F., Kycia, S. & Billinge, S. J. L. (1999). *Phys. Rev. Lett.* **83**, 4089–4092.
Petkov, V., Trikalitis, P. N., Božin, E. S., Billinge, S. J. L., Vogt, T. & Kanatzidis, M. G. (2002). *J. Am. Chem. Soc.* **124**, 10157–10162.
Pradhan, S. K., Bid, S., Gateshki, M. & Petkov, V. (2005). *Mater. Chem. Phys.* **93**, 224–230.
Proffen, T. & Billinge, S. J. L. (1999). *J. Appl. Cryst.* **32**, 572–575.
Qiu, X., Božin, E. S., Juhas, P., Proffen, T. & Billinge, S. J. L. (2004). *J. Appl. Cryst.* **37**, 110–116.
Rietveld, H. M. (1969). *J. Appl. Cryst.* **2**, 65–71.
Rodríguez-Carvajal, J. (1993). *Physica B*, **192**, 55–69.
Šepelák, V., Baabe, D., Mienert, D., Litterst, F. J. & Becker, K. D. (2003). *Scr. Mater.* **48**, 961–966.
Šepelák, V., Menzel, M., Becker, K. D. & Krumeich, F. (2002). *J. Phys. Chem. B*, **106**, 6672–6678.
Stanley, H. E. (1971). *Introduction to Phase Transitions and Critical Phenomena*, p. 263. Oxford: Clarendon Press.
Sugimoto, M. (1999). *J. Am. Ceram. Soc.* **82**, 269–280.
Toby, B. H. & Egami, T. (1992). *Acta Cryst.* A**48**, 336–346.
Vestal, C. R. & Zhang, Z. J. (2004). *Int. J. Nanotechnol.* **1**, 240–263.
Wang, L., Zhou, Q. & Li, F. (2004). *Phys. Status Solidi. B*, **241**, 377–382.
Willey, R. J., Noirclerc, P. & Busca, G. (1993). *Chem. Eng. Commun.* **123**, 1–16.
Young, R. A. (1996). Editor. *The Rietveld Method.* New York: Oxford University Press.